Physics – Uspekhi **66** (9) 943 – 950 (2023)

INSTRUMENTS AND METHODS OF INVESTIGATION PACS numbers: **07.85. – m**, **61.72. – y**, 61.72.Bb

New approaches to three-dimensional dislocation reconstruction in silicon from X-ray topo-tomography data

D A Zolotov, V E Asadchikov, A V Buzmakov, V V Volkov,
I G Dyachkova, P V Konarev, V A Grigorev, E V Suvorov

DOI: https://doi.org/10.3367/UFNe.2022.05.039199

Contents

Abstract. We present the results of processing the diffraction patterns of dislocation half-loops in Si(111) silicon single crystal, which were recorded by X-ray topo-tomography (XTT) at the European Synchrotron Radiation Facility (ESRF). An algorithm for preprocessing two-dimensional images by automatic noise filtering was proposed and solution reliability criteria were developed, which enabled a significant improvement in the quality of three-dimensional reconstruction of the spatial distribution of the defects under study. The experimental patterns were compared with those simulated numerically using the solution of Takagi equations. This approach made it possible not only to determine the geometry of the defects but also to derive information about the Burgers vector.

Keywords: synchrotron radiation, topo-tomography, dislocation half-loops, silicon single crystal, Takagi equations

1. Introduction

A wealth of papers [1–6] are devoted to the study of lattice defects and their influence on physical semiconductor properties, and attention to this area of physics has not eroded. On the one hand, interest in it is growing due to the widespread use of semiconductors, in particular silicon, in the microelectronics industry. On the other hand, modern technologies have stimulated fundamental research in this field. In particular, the technological process of making silicon integrated circuits invites, in some cases, the controlled introduction of extended defects (for example, dislocations) into silicon, since they are excellent getters and are used to effectively clean the working layer of silicon wafers from harmful impurities [7–9]. Dislocations can help solve another problem of modern silicon electronics, namely the production of silicon light emitting diodes (LEDs) inside chips for optoelectronic communication, which are currently not efficient enough. One of the applications is the use of dislocation luminescence by way of controlled dislocation generation in a strictly defined area of silicon [10–12]. Finally, studying the properties of dislocations in silicon was required for the modern power industry, in which silicon containing a large number of dislocations is widely used for the manufacture of solar cells. In this case, dislocations strongly affect the lifetime of minority current carriers and largely determine the energy yield of solar batteries [13, 14].

Solving these problems calls for obtaining detailed information about the structural state of bulk single crystals, in particular, about the mechanisms of generation and distribution of dislocations. As is well known, electron and X-ray microscopy techniques are usually used to assess structural perfection. The advantage of using X-ray methods is that they enable obtaining information about the internal structure of large (up to several cubic millimeters) crystals in a nondestructive way. One of the currently available and most promising methods for studying bulk single crystals is X-ray topo-tomography (XTT), and for studying flat single-crystal samples, for example, plates, X-ray diffraction laminography [15]. The main idea behind these approaches is the combination of X-ray diffraction [16–18] and computed tomography [19]. XTT refers to direct methods for studying the real structure of crystals, which extract information about defects from their diffraction images (topograms) obtained in the Laue geometry for various angles of sample rotation [20–22].

D A Zolotov [1,*], **V E Asadchikov** [1], **A V Buzmakov** [1], **V V Volkov** [1], **I G Dyachkova** [1], **P V Konarev** [1], **V A Grigorev** [1,2], **E V Suvorov** [3]
[1] Federal Scientific Research Center Crystallography and Photonics, Russian Academy of Sciences, Leninskii prosp. 59, 119333 Moscow, Russian Federation
[2] National Research Nuclear University MEPhI (Moscow Engineering Physics Institute), Kashirskoe shosse 31, 115409 Moscow, Russian Federation
[3] Institute of Solid State Physics, Russian Academy of Sciences, ul. Akademika Osip'yana 2, 142432 Chernogolovka, Moscow region, Russian Federation
E-mail: [*] zolotovden@crys.ras.ru

Received 28 March 2022, revised 25 April 2022
Uspekhi Fizicheskikh Nauk **193** (9) 1001 – 1009 (2023)
Translated by E N Ragozin

The nature of the sensitivity of XTT to defects in crystals is deformational; the method reacts to defects that distort the periodic structure of the crystal lattice. Although the formation mechanism of diffraction images of defects is complex, the images themselves are quite clear and allow not only obtaining qualitative information about defects (data on the spatial distribution of defects in the crystal volume) but also quantitatively determining their parameters: the depth of defects, their length, etc.

The range of possible applications of the XTT method is broadening as new and more easily accessible synchrotron stations appear [23]. At present, it is possible, for example, to study the spatial distribution and plastic deformation of grains in polycrystals [24–26], visualize the growth of cracks [27], and study *in situ* the growth of crystals, as well as the nucleation and motion of defects [28]. In combination with the use of X-ray optics, such as compound refractive lenses, it became possible to study individual dislocations with nanometer-high spatial resolution [29]. Particular attention is paid to the study of the nucleation and motion of dislocation loops resulting from mechanical and thermal action on a silicon platelet [30, 31]. Hänschke et al. [31] described visualization of dislocation loops and indexing of their Burgers vectors, which was performed by correlating the data of two independent X-ray diffraction experiments in combination with visible light microscopy.

In this work, XTT is used to reveal the spatial arrangement of single dislocation half-loops in an Si(111) single crystal with a spatial resolution of about 1 μm using monochromatic X-ray radiation from a synchrotron source under weak beam conditions [32]. The linear defects under study were introduced using a four-point bending method [33]; in this case, two types of dislocations can arise, lying in the slip planes $(\bar{1}11)$ and/or $(1\bar{1}1)$ with the Burgers vectors $[0\bar{1}1]$ and $[101]$.

Note that the currently used mathematical algorithms for processing topo-tomography data are a development of absorption tomography methods, which do not make it possible to accurately include the propagation of radiation in a crystal and, therefore, interpret the effects of the phase-amplitude image contrast. This paper proposes a combined approach that allows us to detect defects in crystals by traditional methods and then compare them with the data of numerical simulation of diffraction images. The implementation of this approach is possible due to the use of a few-parameter description of localized microdefects in crystals and the reconstruction of the corresponding parameters from a set of experimentally recorded X-ray images. To this end, the existing algorithms for processing experimental data were modified and software was developed for modeling images of microsized defects in crystals.

In our work, modern methods of digital image processing were applied to interpret experimental data. Such high-resolution three-dimensional (3D) reconstruction methods are sensitive to noise in projection data obtained even using synchrotron radiation. One of the possible ways to improve the quality of 3D defect images developed in this study involves preliminary processing of experimental projection images with automatic noise filtering, the separation of images of dislocation half-loops based on a statistical analysis of the intensity distribution and image structure, and the application of solution reliability criteria. To improve the quality of 3D reconstruction and minimize the effect of artifacts, topographic images were reconstructed employing widely used algebraic methods (Algebraic Reconstruction Techniques, ART) [19] adapted to the geometry of the X-ray diffraction experiment.

The paper also presents the results of dislocation half-loops modeling based on the tools of the X-ray diffraction theory, in particular, the Takagi equations. Previously, individual linear dislocations were modeled using these equations [34], but they were valid only for an infinite dislocation. For a more correct comparison of the experimental data with the simulation results, the expression for the displacement field was modified with the inclusion of dislocation half-loop geometry.

2. Methods

2.1 X-ray diffraction measurements

An Si(111) single crystal measuring $50 \times 3.55 \times 0.78$ mm with artificially introduced dislocation half-loops was chosen as the subject under study [21, 22]. The experiment was carried out using a mobile X-ray diffraction complex developed at the Karlsruhe Institute of Technology (German: Karlsruher Institut für Technologie, KIT) and put into operation at the ID19 station of the ESRF (European Synchrotron Radiation Facility) synchrotron source (Grenoble, France). Use was made of an approximately 2×2-mm-sized X-ray beam monochromatized to 23.567 keV using a two-crystal Si(111) monochromator. Two-dimensional diffraction projections were measured using a recording system with an effective pixel size of 0.96 μm. The system consisted of a 25-μm-thick LuAG crystal, a 6.5-μm pixel AndorNeo camera, and a $\times 7.5/\times 0.9$ tubular lens. A dataset of 100 projection images was obtained at equal angular intervals during the rotation of the sample by 360° around the diffraction vector $\mathbf{h}$ $[2\bar{2}0]$.

2.2 Noise filtration and smoothing of two-dimensional tomographic projections

A feature of tomographic measurements is the impossibility of recording the direct diffracted beam or its analogue (obtained using the standard flat-field correction procedure), which could be used to correct the background and reduce the noise of topo-tomographic projections. Therefore, in this paper, we propose a nonparametric statistical method for analyzing topo-tomographic projections to separate the noise component of the background (scattered radiation, detector dark current, etc.) from the useful signal, which makes it possible to reduce the influence of the subjective assessment of the researcher on the filtering result. To this end, a program was developed for effective noise suppression of experimental XTT data based on the least squares method with regularization and adaptive weighting reliant on the results of their statistical analysis. In particular, the paper proposes a nonparametric smoothing approach with a Hamming kernel [35] in a two-dimensional implementation. The results of filtering using other well-known algorithms largely depend on the accuracy of estimating the noise variance in the initial data.

In this work, advantage was taken of the smoothing method without using a priori estimates of the variance. The main criterion for the solution quality was the magnitude of the autocorrelation of the differences w_i between the initial z_i and smoothed s_i intensities, $w_i = z_i - s_i$, which should correspond to a sample from a random sequence. The most suitable estimate was the Durbin–Watson autocorrelation test (or DW-criterion) [36] applied to a sequence of N

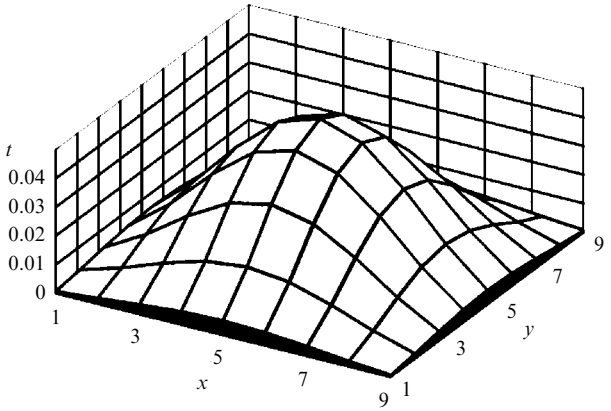

Figure 1. Example of the shape of the weight function (kernel) of smoothing for a window of 9×9 pixels. The x- and y-axes show the indices of points in the scanning window, and the z-axis shows the values of the normalized weight function. The smoothed value is obtained at the point with indices 5,5.

differences w_i within a scanning window ranging in size from 3×3 to 9×9 pixels:

$$\mathrm{DW} = 2 - 2\,\frac{\sum_{i=2}^{N} w_i w_{i-1}}{\sum_{i=1}^{N} w_i^2}\,. \qquad (1)$$

The sequence of values w_i in the window ($i = 1, 2, \ldots, N$, $N = M^2$, where M is the linear size of the square window) was obtained by the reciprocating raster method, i.e., after sampling was completed from the current row of differences in the window, the next row was scanned in the opposite direction in order to preserve the step length between adjacent pixels. The degree of smoothing was considered acceptable if the criterion value averaged over the image was in the range of 1.7–2.2, which corresponded to the 95% significance level of the hypothesis about the absence of autocorrelation between the intensities of differences in adjacent pixels. A two-dimensional analogue of the nonparametric method with a Hamming kernel (weight window) was used for smoothing. [35]. The smoothed value s at the central point of the scanning window was obtained as an average value calculated with a weight proportional to the value of the rasterized, as described above, bell-shaped function t_i, $i = 1, \ldots, N$, having a generatrix with the shape of one period of the cosine shifted vertically to the positive region with the center coinciding with the center of the window (Fig. 1): $s = \sum_{i=1}^{N} z_i t_i$. Weight function t_i was normalized to the unit sum of its values.

The degree of smoothing was controlled by varying the size of the scan window. This size, which depends on the resolution of the image, ranged from 3 to 11 pixels in this work. For additional verification of the result, use was made of several semi-empirical criteria reliant on an analysis of the curvature of the smoothed surface (the criterion was the value of the total second derivative calculated from the finite differences on the grid in the scanning window) and the relative value of the systematic component in the residuals (the ratio of the norms of the initial data arrays to the smoothed differences between original and smoothed data).

Figures 2a and 2b show an X-ray diffraction image of a silicon crystal domain containing a cluster of dislocation half-loops. As one can see from Fig. 2c, a significant decrease in the background noise component was obtained after applying the algorithm developed.

2.3 Topo-tomographic reconstruction

To perform the topo-tomographic reconstruction, we used the assumption that the image from the crystal under study was formed in the Laue geometry, when the angle of incidence of the radiation was equal to the angle of reflection. To simplify the description of the measurement geometry, a virtual X-ray source was introduced, the rays from which were shifted by a double Bragg angle relative to the real source (Fig. 3).

Let the beam in the xz plane fall on the object at the Bragg angle θ_B to the x-axis; the reflected beam then lies in the xz plane. The object rotates about the z-axis at angular increments of φ. We introduce the following notation: $P_\varphi(y, z)$ is the experimental X-ray image (intensity at detector point (y, z)) obtained at the object rotation angle φ; $X_n(x, y, z)$ is the object being reconstructed (three-dimensional distribution of the object reflectivity) at the nth iteration; $X_n^\varphi(x, y, z)$ is the $X_n(x, y, z)$ object rotated by the angles φ and θ_B; and $P'_\varphi(y, z)$ is the calculated image of the object X_n^φ (intensity at detector point (y, z)).

The task of topo-tomographic reconstruction is to find an object X_n such that its projections are as similar as possible to the measured ones, i.e., it is necessary to solve the optimization problem for all rotation angles of the object φ:

$$\left\| P_\varphi(y, z) - P'_\varphi(y, z) \right\|^2 \underset{\varphi}{\rightarrow} \min\,.$$

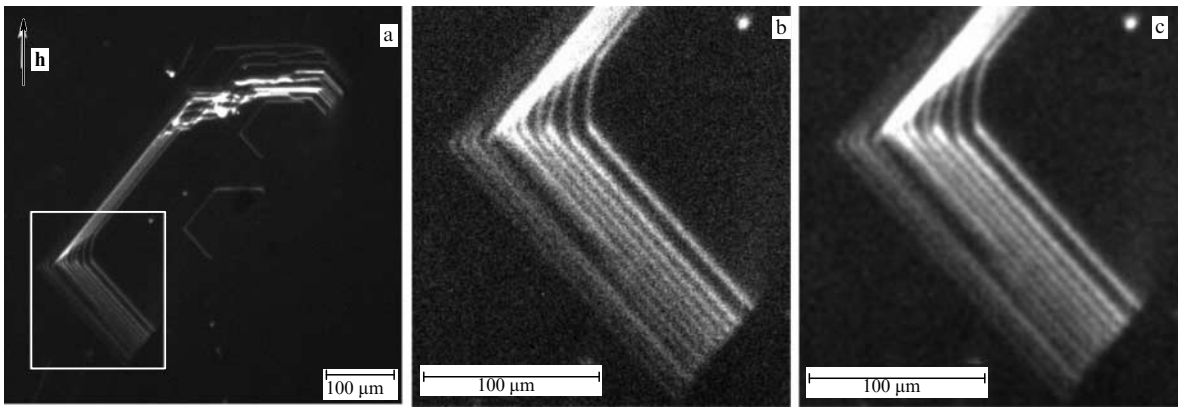

Figure 2. X-ray topograms of defects in the Si(111) single crystal under study: (a) initial topogram; (b) an enlarged part containing a bunch of dislocations; (c) topogram after applying background signal smoothing using the Hamming kernel. Arrow shows the direction of diffraction vector **h**.

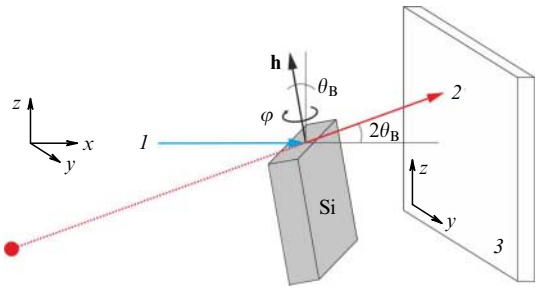

Figure 3. Schematic of the topo-tomographic experiment. *1* — monochromatic beam, *2* — diffracted beam, *3* — two-dimensional detector, φ — sample rotation angle, θ_B — Bragg angle, **h** — diffraction vector.

This problem was solved using the Conjugate Gradient method for Least Squares (CGLS) implemented in the ASTRA Toolbox software package [37].

To obtain a high-quality tomographic reconstruction, it is necessary to correctly determine the position of the axis of rotation. When the rotation axis is perpendicular to the X-ray beam, the search for the axis is performed by combining opposite images, i.e., those obtained at angles of 0 and 180° [38]. In the case of topo-tomography, the axis of rotation is tilted at the double Bragg angle, so the resultant opposite projections can differ significantly (Fig. 4). However, one can see from Fig. 4 that, although points on opposite projections may be shifted vertically along the axis of rotation of the object, their horizontal distance to the axis of rotation is preserved. To search for the position of the rotation axis in the crystal images, several characteristic points were selected so that they could be visually identified in different images of the object. These points were used to find the axis of rotation as a straight line lying at an equal distance from the characteristic points on opposite projections.

2.4 Simulation of topo-tomographic experiment

We used the Takagi equations [39] to simulate the topo-tomographic experiment:

$$\begin{aligned} -\frac{2\mathrm{i}}{k}\frac{\partial D_0(\mathbf{r})}{\partial s_0} &= \chi_0 D_0(\mathbf{r}) + C\chi_{\bar{h}} D_h(\mathbf{r}) \exp\left(-\mathrm{i}\mathbf{h}\mathbf{u}(\mathbf{r})\right), \\ -\frac{2\mathrm{i}}{k}\frac{\partial D_h(\mathbf{r})}{\partial s_h} &= (\chi_0 - \alpha) D_h(\mathbf{r}) + C\chi_h D_0(\mathbf{r}) \exp\left(-\mathrm{i}\mathbf{h}\mathbf{u}(\mathbf{r})\right), \end{aligned} \tag{2}$$

where k is the wavenumber, χ_0, χ_h, and $\chi_{\bar{h}}$ are the Fourier components of the crystal polarizability for the transmitted and diffracted waves, D_0 and D_h are the amplitudes of the transmitted and diffracted waves, $\partial/\partial s_0$ and $\partial/\partial s_h$ are derivatives with respect to the directions of the transmitted and diffracted waves, respectively, coefficient $C = 1$ for σ-polarization and $C = \cos(2\theta_B)$ for π-polarization, **h** is the diffraction vector, $\mathbf{u}(\mathbf{r})$ is the vector of the displacement (strain) field, and α is the deviation from the exact Bragg condition:

$$\alpha = \frac{k_h^2 - k_0^2}{k_0^2}. \tag{3}$$

Equations (2) describe the wave field propagation in the bulk of the crystal. To calculate the wave amplitudes, we used triangular grids constructed on the unit vectors of the transmitted and diffracted waves in the skew coordinate system (X, Y, S) (Fig. 5). In this coordinate system, Eqns (2) assume the form

$$\begin{aligned} D_0(X,S) &= D_0(X+p, S-p) \\ &\quad + A\left[D_h(X,S) + D_h(X+p, S-p)\right], \\ D_h(X,S) &= D_h(X, S-p) + B\left[D_0(X,S) + D_0(X, S-p)\right] \\ &\quad + D_h(X,S)W(X,S) + D_h(X,S-p)W(X,S-p), \end{aligned} \tag{4}$$

where the following notation is introduced:

$$\begin{aligned} A &= \frac{pkC\chi_{\bar{h}}}{4\mathrm{i}}, \quad B = \frac{pkC\chi_h}{4\mathrm{i}}, \\ W(X,Y,S) &= -\frac{pk\alpha}{4\mathrm{i}} - \frac{p}{2\mathrm{i}}\frac{\partial\left(\mathbf{h}\mathbf{u}(X,Y,S)\right)}{\partial S}. \end{aligned} \tag{5}$$

The equations also contain the diffraction vector **h** scalarly multiplied by the displacement field vector **u** characterizing the dislocation [40]:

$$\begin{aligned} \mathbf{u}(r_0) &= \frac{\mathbf{b}}{2\pi}\arctan\frac{z_0}{y_0} + \frac{\mathbf{b} - \boldsymbol{\tau}(\mathbf{b}\boldsymbol{\tau})}{2\pi}\frac{y_0 z_0}{2(1-\nu)(y_0^2+z_0^2)} \\ &\quad - \frac{\boldsymbol{\tau}\times\mathbf{b}}{2\pi}\left(\frac{1-2\nu}{4(1-\nu)}\ln(y_0^2+z_0^2) + \frac{y_0^2 - z_0^2}{4(1-\nu)(y_0^2+z_0^2)}\right). \end{aligned} \tag{6}$$

Expression (6) uses the following notation: **b** is the Burgers vector, $\boldsymbol{\tau}$ is a unit vector parallel to the dislocation line, and ν is Poisson's ratio. The equation is given in a rectangular coordinate system (x_0, y_0, z_0), where the x_0-axis is

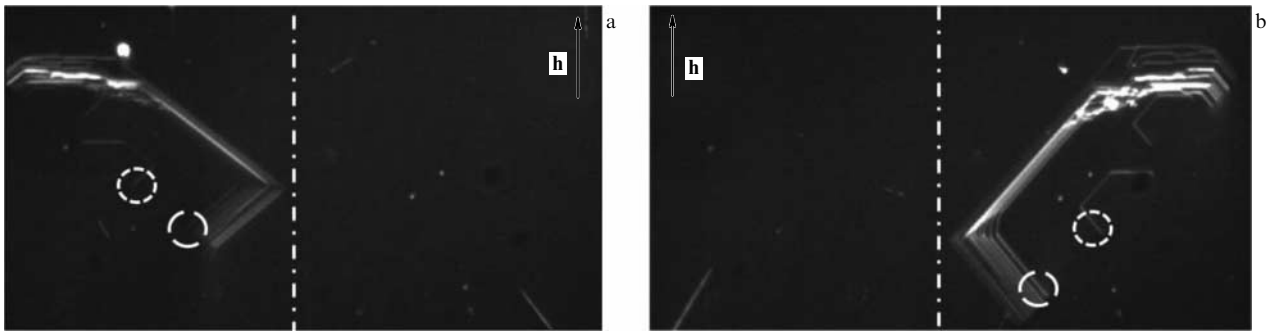

Figure 4. Search for the axis of rotation of the object under study. Shown are the dislocation images obtained at rotation angles (a) 0 and (b) 180°. Dashed circles mark the characteristic points that were used to determine the position of the axis. Vertical dashed-dotted straight line is the rotation axis of the object.

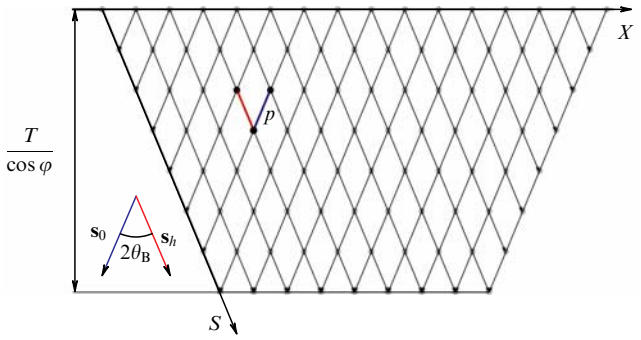

Figure 5. Triangular grid for calculating wave amplitudes constructed in the skew coordinate system (X, Y, S) (Y-axis is perpendicular to the plane of Fig. 5). φ is the sample rotation angle, T is the plate thickness, p is the grid step corresponding to the resolution of the original topogram (0.96 μm), $\mathbf{s}_0$ and $\mathbf{s}_h$ are unit vectors along directions of incident and diffracted waves.

directed along the $\boldsymbol{\tau}$ vector, and the z_0-axis is directed along the $\boldsymbol{\tau} \times \mathbf{b}$ vector.

The so-defined displacement field describes an infinite rectilinear dislocation. To describe dislocation structures consisting of several straight dislocations, the displacement field of each dislocation is limited by the window function $w(x_0, y_0, z_0)$. Then, the expression for the displacement field of the dislocation structure takes on the form

$$\mathbf{u} = \mathbf{u}_1 w_1 + \mathbf{u}_2 w_2 + \ldots + \mathbf{u}_n w_n \,, \tag{7}$$

where n is the number of dislocations that make up the dislocation structure; each term is given in its own coordinate system: $\mathbf{u}_k = \mathbf{u}_k(x_{0k}, y_{0k}, z_{0k})$, $w_k = w_k(x_{0k}, y_{0k}, z_{0k})$. How the coordinate systems (x_0, y_0, z_0), (x, y, z), and (X, Y, S) are related is described in detail in Ref. [41].

3. Results and discussion

The use of the developed algorithms and programs for efficient automatic noise filtering and two-dimensional tomographic projection smoothing using the criteria for the autocorrelation of differences made it possible to carry out a three-dimensional (3D) reconstruction of dislocation half-loop clusters in an Si(111) crystal (Fig. 6). An indisputable advantage of the XTT method over conventional two-dimensional projection topography is the possibility of separating out almost any section from a three-dimensional

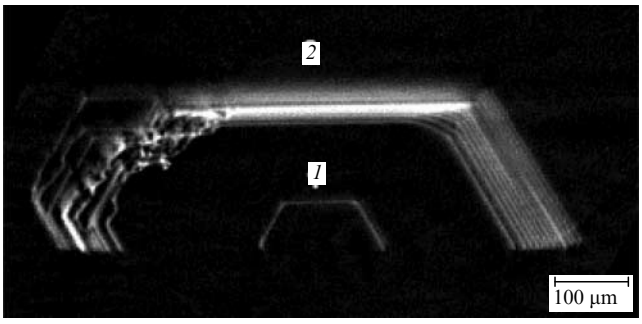

Figure 6. Result of a three-dimensional reconstruction of the spatial arrangement of a dislocation half-loop cluster in an Si(111) single crystal after applying the filtering procedure. $(1\bar{1}1)$ slip plane is shown. *1* is a single dislocation, *2* corresponds to a bunch of dislocation half-loops.

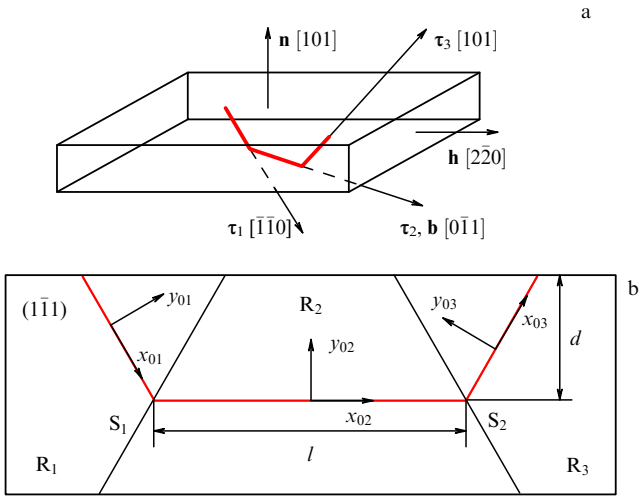

Figure 7. Schematic representation of a dislocation half-loop in the $(1\bar{1}1)$ plane. (a) General view: $\mathbf{n}$ is the normal vector to the surface of the crystal plate, $\mathbf{h}$ is the diffraction vector, $\boldsymbol{\tau}_{1,2,3}$ are directions of dislocation portions. (b) Slip plane containing the half-loop: S_1, S_2 are planes separating dislocation segments; R_1, R_2, R_3 are regions of space separated by planes S_1, S_2 and the surface of the crystal.

volume. In particular, slip planes $(1\bar{1}1)$ were identified, in the images of which the half-loops under study were clearly discernible. Figure 6 (image *1*) clearly shows a single dislocation loop. In addition, a defect is located in the same plane, consisting of at least 12 single dislocations densely spaced relative to each other (image *2* in Fig. 6). These images were subsequently used to estimate the geometric dimensions of the defects under study and their subsequent simulation.

A single dislocation half-loop was used for simulation (image *1* in Fig. 6). A schematic representation of a half-loop consisting of three segments is shown in Fig. 7a.

The geometry of this half-loop is such that the angle between the neighboring dislocations is 120°. In order to construct a window function for each of the dislocations, we draw two planes, S_1 and S_2, through the intersection points of neighboring dislocation segments perpendicular to the half-loop plane (Fig. 7b). For ease of calculation, the planes are chosen so that they make equal angles of 60° with the dislocation lines. The window function assumes a value equal to either unity or zero, depending in which region of space the given point belongs. For example, if the point considered belongs in the space bounded by the S_1 plane and the crystal surface (domain R_1 in Fig. 7b), then the window functions assume the following values: $w_1 = 1$, $w_2 = 0$, $w_3 = 0$. Therefore, Eqn (7) can be represented as

$$\mathbf{u}(\mathbf{r}) = \begin{cases} \mathbf{u}_1(x_{01}, y_{01}, z_{01}) \,, & \text{if } \mathbf{r} \in R_1 \,, \\ \mathbf{u}_2(x_{02}, y_{02}, z_{02}) \,, & \text{if } \mathbf{r} \in R_2 \,, \\ \mathbf{u}_3(x_{03}, y_{03}, z_{03}) \,, & \text{if } \mathbf{r} \in R_3 \,. \end{cases} \tag{8}$$

The displacement field defined in this way describes the entire dislocation half-loop. However, in order to unambiguously define the half-loop, it is necessary to introduce its geometric dimensions. In this case, we used the length of the middle dislocation l and its distance from the crystal surface d. Since side dislocations emerge on the crystal surface, these parameters are sufficient to determine their length. The required dimensions of the half-loop, $d = 63$ μm, $l = 100$ μm, were determined from tomographic images after its 3D reconstruction (see Fig. 6).

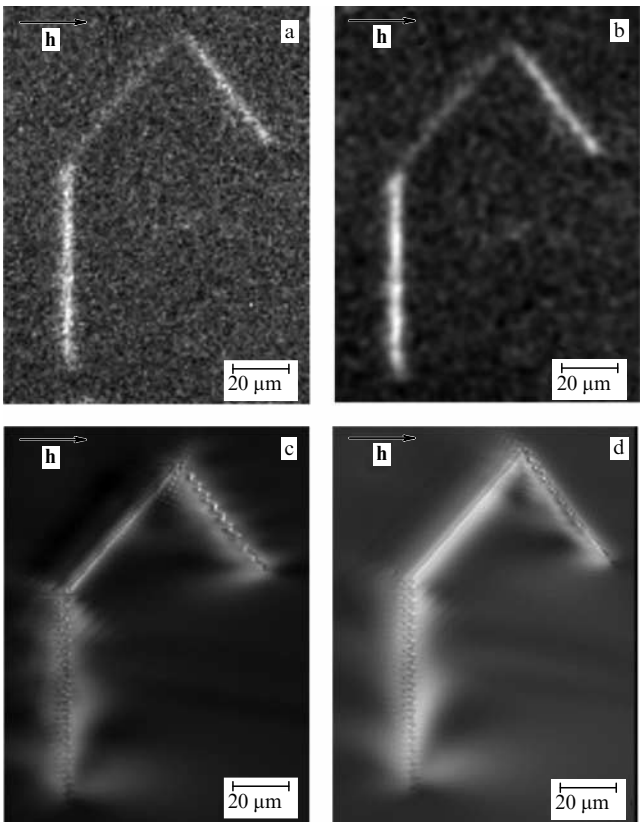

Figure 8. Diffraction images of a dislocation half-loop: (a) initial experimental data, (b) experimental data after filtering, (c) model topogram with the Burgers vector $[0\bar{1}1]$, (d) model topogram with the Burgers vector [101].

The numerical solution of the equations was based on the program code, whose algorithm is described at length in Ref. [41]. The solutions of the equations are the amplitudes of the transmitted D_0 and diffracted D_h waves in the bulk of the crystal. The displacement fields $\mathbf{u}(\mathbf{r})$ of each individual dislocation are linked into a single expression to describe the entire half-loop. In this case, the displacement field was artificially limited by the length of the middle portion of the dislocation and its depth. Since the radiation enters the detector upon exiting the crystal, the intensity distribution on the output surface of the sample is taken as the topogram. However, for nonzero values of the rotation angle φ, the output plane of the plate is not parallel to the detector surface, and such a pattern does not correspond to the experimental image. To take into account this circumstance, a correction was introduced to project the image along the direction of diffracted radiation.

Model topograms were calculated for two Burgers vectors, $[0\bar{1}1]$ and [101], for a single dislocation loop, whose directions are shown in Fig. 7. Simulations were carried out for the angle of rotation $\varphi = 302.4^\circ$ and the parameter α in the range from -0.004° to 0.004°. Experimental images and simulation results are shown in Fig. 8.

For a criterion of the correspondence between the experimental and model topograms, we employed the convergence parameter L:

$$L^2 = \left(\sum_{i=1}^{n} (I_{\mathrm{exp},i} - I_{\mathrm{calc},i})^2\right)\left(\sum_{i=1}^{n} I_{\mathrm{calc},i}^2\right)^{-1}, \qquad (9)$$

where I_{exp} and I_{calc} are the intensities of the experimental and model topograms, and n is the number of image pixels.

The values of the L^2 factor were calculated according to formula (9). For the Burgers vector $[0\bar{1}1]$, the L^2 factor was 1.133, while for the Burgers vector [101], it was 1.155. Both figures indicate good agreement between the model topograms. However, one can see from the images that the intensity from the middle part of the dislocation loop in the experimental image is much weaker than from the side ones. The same is observed in the case of the model topogram for the Burgers vector $[0\bar{1}1]$. Consequently, the observed dislocation half-loop in the experimental topogram has the Burgers vector $[0\bar{1}1]$. This result is confirmed by the data obtained previously in Ref. [22].

To simulate topograms of more complex structures, such as a bunch of dislocation loops, one has to know the position in space of each of the half-loops, which depends on the direction $\boldsymbol{\tau}$ of each dislocation, the depth d, and the length of the middle dislocation l. Furthermore, the displacement field can have a very complex structure, but for the sake of simplicity of simulations we can assume that the displacement field at a given point is a vector sum of the displacement fields of individual dislocation loops. The displacement field of the dislocation bunch can then be represented as

$$\mathbf{u}(\mathbf{r}) = \sum_{i=1}^{m} \mathbf{u}_i(\mathbf{r}), \qquad (10)$$

where m is the number of dislocation loops, and $\mathbf{u}_i(\mathbf{r})$ is the displacement field of an individual half-loop given by expressions (6) and (7).

To unambiguously determine the orientation of the bunch in the crystal, it only remains to find the length of the middle dislocation segment l for each half-loop from the bunch and the depth d. To this end, as in the case of a single dislocation, the 3D model (Fig. 9a) was used to determine the depth range of the dislocation structure, which was $166 < d < 200$ μm. Since the central segments of dislocations cannot be resolved, their depth was determined by the following algorithm. Based on the intensity profile of the topogram of side dislocations (Fig. 9b), their positions D_i $(i = 1, 2, \ldots, 12)$ are found relative to the conventional point (see Table). Since the dislocation loops are geometrically similar to each other, the ratio of the distances between the middle segments is equal to the ratio of the distances between the corresponding side segments. Therefore,

$$\frac{d_i - d_1}{d_n - d_1} = \frac{D_i - D_1}{D_n - D_1}, \quad i = 1, 2, \ldots, n, \quad n = 12, \qquad (11)$$

Table. Positions D of dislocation side segments and depths d.

Dislocation number i	D, μm	d, μm
1	10.5	166.0
2	26.9	171.9
3	35.5	174.9
4	44.2	178.0
5	49.9	180.1
6	57.6	182.8
7	65.3	185.6
8	73.0	188.3
9	80.6	191.1
10	90.2	194.5
11	97.9	197.2
12	105.6	200.0

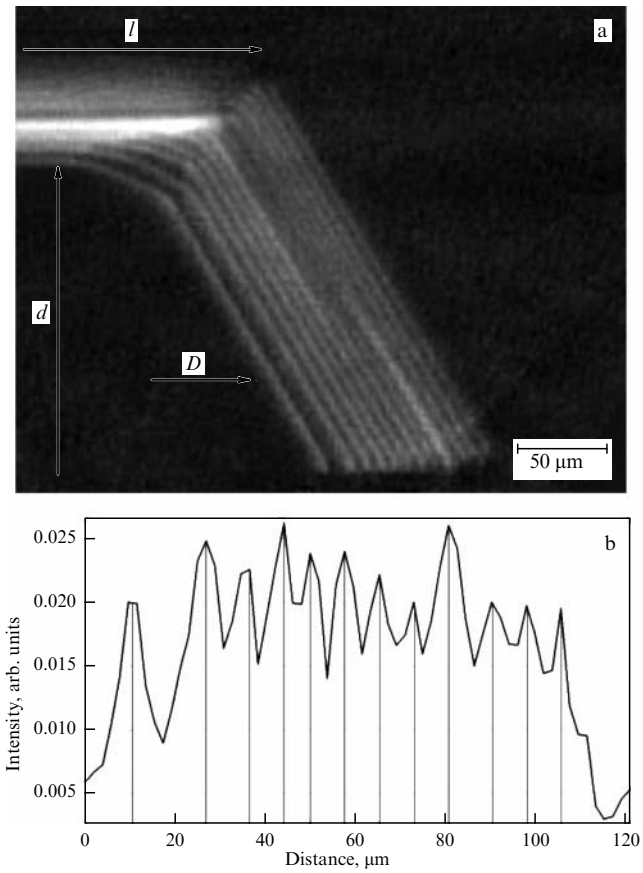

Figure 9. (a) Part of a bunch of dislocation loops. Illustration shows the proportionality of the length of middle dislocation l to depth d. (b) Intensity profile of the topogram of side dislocations for determining positions D between them.

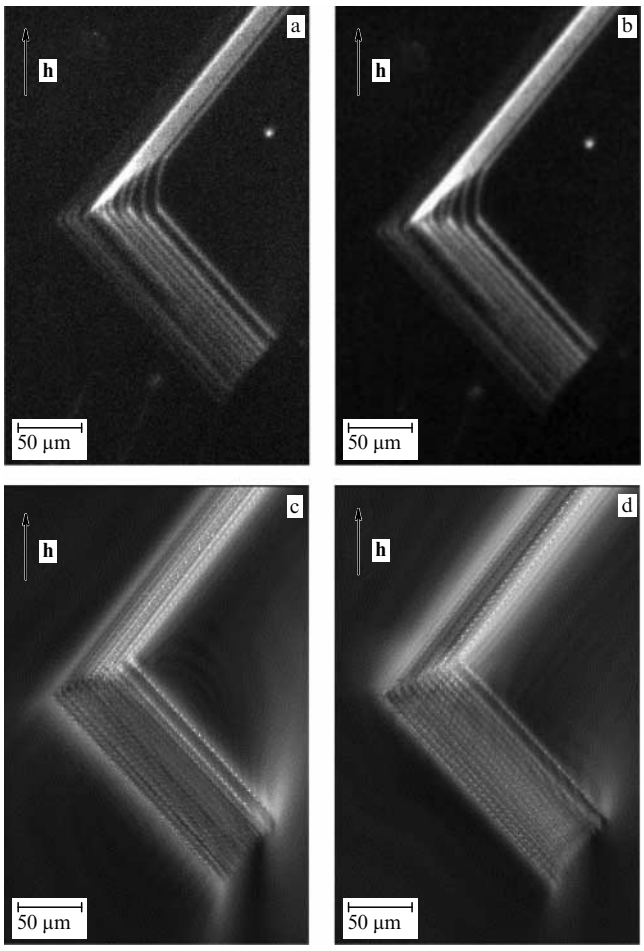

Figure 10. Topographic images of a part of a bunch of dislocation loops for angle $\varphi = 122.4°$: (a) experimental, (b) filtered from noise, (c) model with Burgers vector $\mathbf{b} = [0\bar{1}1]$, (d) model with Burgers vector $\mathbf{b} = [101]$. Topogram pixel size is 0.96 μm.

where d_i is the depth of the ith middle dislocation ($d_1 = 166$ μm, $d_n = 200$ μm), and D_i is the position of the ith side dislocation. In formula (11), only the depths d_i are unknown, and their values are calculated and displayed in the Table.

Figures 10 and 11 show the experimental and corresponding model topograms before and after noise filtering for angles $\varphi = 122.4°$ and 316.2°. The choice of rotation angles is determined from the point of view of contrast, clarity of their structure, and the absence of extraneous crystal defects in the immediate vicinity of the selected dislocation fragment. One can see that, for different Burgers vectors, the topograms differ in contrast. The middle dislocation segments for the Burgers vector $\mathbf{b} = [0\bar{1}1]$ have sharper boundaries than for the Burgers vector $\mathbf{b} = [101]$. It is noteworthy that the left side of the studied closely spaced defects has a more complex tortuous structure (see Fig. 6) and was not considered in this simulation.

To date, the determination of the direction of the Burgers vector of a dislocation has been based on the decrease in the intensity of a diffraction image that satisfies the condition $\mathbf{hb} = 0$ (here, $\mathbf{h}$ is the diffraction vector and $\mathbf{b}$ is the Burgers vector). In this paper, we propose a method for determining the direction of the Burgers vector of a dislocation half-loop in an Si(111) silicon single crystal by comparing experimental topograms obtained by XTT and their model analogs at different crystal rotation angles. To do this, two parameters were extracted from the reconstructed 3D model of the cluster of dislocation half-loops which were used in the simulation: the length of the middle segment of the dislocation and its distance to the nearest surface of the silicon plate (the middle segment of the dislocation was parallel to the surface of the single crystal).

4. Conclusions

The set of methods developed for processing X-ray diffraction tomography data, which comprises preliminary processing of experimental images by automatic noise filtering and criteria for the reliability of the solution, has significantly improved the quality of the three-dimensional reconstruction of the spatial arrangement of a cluster of dislocation half-loops in an Si(111) single crystal.

Furthermore, a mathematical apparatus based on the Takagi equations has been developed, which permits modeling two-dimensional topographic images of dislocation structures to determine their quantitative characteristics. For the purpose of testing, this approach was applied to dislocation structures in Si(111) with already known parameters. It is shown that the calculated and measured characteristics correspond to each other. We can therefore conclude that the newly developed approach makes it possible to obtain theoretical quantitative estimates of the

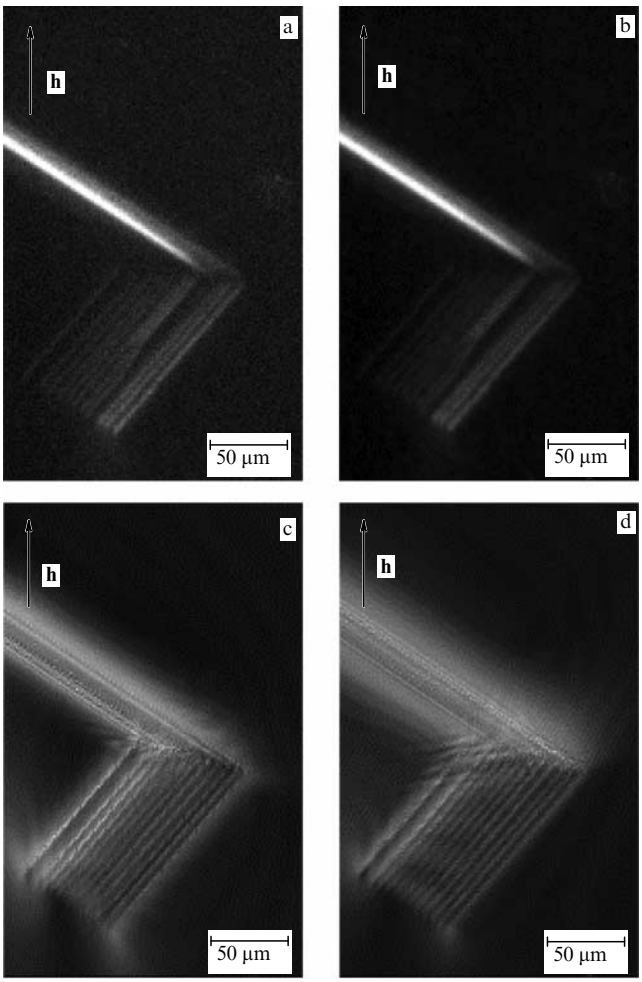

Figure 11. Topographic images of part of a bunch of dislocation loops for angle $\varphi = 316.2°$: (a) experimental, (b) filtered from noise, (c) model with Burgers vector $\mathbf{b} = [0\bar{1}1]$, (d) model with Burgers vector $\mathbf{b} = [101]$. Topogram pixel size is 0.96 μm.

observed contrast from various dislocation structures without performing a complex and time-consuming XTT experiment.

In general, such an approach to projection data processing makes it possible to solve the problems of interpreting images in diffraction tomography to reconstruct three-dimensional elastic displacement fields of microsized defects, which in turn makes it possible to reconstruct the geometry of 3D dislocation structures in a volume of single crystals. The solution to this problem is sought after in the development of new functional materials.

Acknowledgements

This study was performed in the framework of the state assignment of the Federal Research Center Crystallography and Photonics of the Russian Academy of Sciences in terms of ''application of tomographic algorithms'' and with the support of the Russian Foundation for Basic Research (projects 19-02-00556 A, 18-29-26036 mk) in terms of ''processing, filtering experimental data.''

The authors express their appreciation to Daniel Hänschke, Simon Bode, Merve Kabukcuoglu, and Elias Hamann of the Karlsruhe Institute of Technology for the research carried out at the ID19/ESRF station within the joint German–Russian project STROBOS-CODE (grant no. 05K14VFA, agreement 14.616.21.0005) and their helpful comments made in the course of this work.

References

1. Reiche M et al. *Appl. Phys. A* **122** 389 (2016)
2. Mahajan S *Acta Mater.* **48** 137 (2000)
3. Reiche M et al. *J. Appl. Phys.* **115** 194303 (2014)
4. Pizzagalli L, Demenet J-L, Rabier J *Phys. Rev. B* **79** 045203 (2009)
5. Asadchikov V E et al. *Semiconductors* **54** 666 (2020); *Fiz. Tekh. Poluprovodn.* **54** 557 (2020)
6. Shevchenko S A, Tereshchenko A N, Mazilkin A A *Izv. Vyssh. Uchebn. Zaved. Mater. Elektron. Tekh.* **17** (3) 211 (2014)
7. Kharchenko V A *Mod. Electron. Mater.* **5** (1) 1 (2019); *Izv. Vyssh. Uchebn. Zaved. Mater. Elektron. Tekh.* **21** (1) 5 (2018)
8. Perevostchikov V A, Skoupov V D *Gettering Defects in Semiconductors* (Springer Ser. in Advanced Microelectronics, Vol. 19) (Berlin: Springer, 2005)
9. Nagornykh S N et al. *Mod. Electron. Mater.* **1** 33 (2015); *Izv. Vyssh. Uchebn. Zaved. Mater. Elektron. Tekh.* **17** (4) 252 (2014)
10. Pavlyk B, Kushlyk M, Slobodzyan D *Nanoscale Res. Lett.* **12** 358 (2017)
11. Sobolev N A *Semiconductors* **44** 1 (2010); *Fiz. Tekh. Poluprovodn.* **44** (1) 3 (2010)
12. Seibt M et al. *Appl. Phys. A* **96** 235 (2009)
13. Cousins P J, Cotter J E *IEEE Trans. Electron Devices* **53** 457 (2006)
14. Prokop'ev E P et al. *Nanotechnol. Res. Practice* **4** 213 (2014)
15. Hänschke D et al. *Appl. Phys. Lett.* **101** 244103 (2012)
16. Authier A *Dynamical Theory of X-ray Diffraction* (IUCr Monographs on Crystallography, Vol. 11) (New York: Intern. Union of Crystallography, Oxford Sci. Publ., 2001)
17. Bowen D K, Tanner B K *High Resolution X-Ray Diffractometry and Topography* (London: CRC Press. Taylor and Francis, 1998)
18. Lider V V *Phys. Solid State* **63** 189 (2021); *Fiz. Tverd. Tela* **63** (2) 165 (2021)
19. Kak A C, Slaney M *Principles of Computerized Tomographic Imaging* (New York: IEEE Press, 1988)
20. Ludwig W et al. *J. Appl. Cryst.* **34** 602 (2001)
21. Zolotov D A et al. *Optoelectron. Instrument. Data Process.* **55** 126 (2019); *Avtometriya* **55** (2) 28 (2019)
22. Asadchikov V et al. *J. Appl. Cryst.* **51** 1616 (2018)
23. Baruchel J et al. *C.R. Phys.* **14** 208 (2013)
24. Ludwig W et al. *J. Appl. Cryst.* **40** 905 (2007)
25. Proudhon H et al. *Materials* **11** (10) (2018) https://doi.org/10.3390/ma11102018
26. Yau A et al. *Science* **356** 739 (2017)
27. Rovinelli A et al. *J. Mech. Phys. Solids* **115** 208 (2018)
28. Zhang J et al. *Acta Mater.* **156** 76 (2018)
29. Poulsen H F et al. *J. Appl. Cryst.* **50** 1441 (2017)
30. Danilewsky A N *Cryst. Res. Technol.* **55** 2000012 (2020)
31. Hänschke D et al. *Phys. Rev. Lett.* **119** 215504 (2017)
32. Peng H et al. *J. Appl. Cryst.* **54** 1225 (2021)
33. Erofeev V N et al. *Sov. Phys. Crystallogr.* **16** 151 (1971); *Kristallografiya* **16** 190 (1971)
34. Indenbom V L, Chukhovskii F N *Sov. Phys. Usp.* **15** 298 (1972); *Usp. Fiz. Nauk* **107** 229 (1972)
35. Durbin J et al. *Biometrika* **58** 1 (1971)
36. Bowman A W, Azzalini A *Applied Smoothing Techniques for Data Analysis. The Kernel Approach with S-Plus Illustrations* (Oxford Statistical Science Ser., Vol. 18) (Oxford: Clarendon Press, 1997)
37. van Aarle W et al. *Opt. Express* **24** 25129 (2016)
38. Buzmakov A V et al. *Bull. Russ. Acad. Sci. Phys.* **83** 146 (2019); *Izv. Ross. Akad. Nauk Ser. Fiz.* **83** 194 (2019)
39. Takagi S *J. Phys. Soc. Jpn.* **26** 1239 (1969)
40. Hirth J P, Lothe J *Theory of Dislocations* (New York: McGraw-Hill, 1968)
41. Besedin I S, Chukhovskii F N, Asadchikov V E *Crystallogr. Rep.* **59** 323 (2014); *Kristallografiya* **59** 365 (2014)